Journal of Colloid and Interface Science 648 (2023) 397–405

Contents lists available at ScienceDirect

Journal of Colloid And Interface Science

journal homepage: www.elsevier.com/locate/jcis

Regular Article

Electrothermoplasmonic flow in gold nanoparticles suspensions: Nonlinear dependence of flow velocity on aggregate concentration

Carlos David González-Gómez [a,b], Raúl A. Rica [a,c], Emilio Ruiz-Reina [b,d,*]

[a] Universidad de Granada, Department of Applied Physics, Nanoparticles Trapping Laboratory, 18071, Granada, Spain
[b] Universidad de Málaga, Department of Applied Physics II, 29071, Málaga, Spain
[c] Universidad de Granada, Research Unit "Modeling Nature" (MNat), 18071, Granada, Spain
[d] Universidad de Málaga, Department of Applied Physics II, Institute Carlos I for Theoretical and Computational Physics (iC1), 29071, Málaga, Spain

ABSTRACT

Efficient mixing and pumping of liquids at the microscale is a technology that is still to be optimized. The combination of an AC electric field with a small temperature gradient leads to a strong electrothermal flow that can be used for multiple purposes. Combining simulations and experiments, an analysis of the performance of electrothermal flow is provided when the temperature gradient is generated by illuminating plasmonic nanoparticles in suspension with a near-resonance laser. Fluid flow is measured by tracking the velocity of fluorescent tracer microparticles in suspension as a function of the electric field, laser power, and concentration of plasmonic particles. Among other results, a non-linear relationship is found between the velocity of the fluid and particle concentration, which is justified in terms of multiple scattering-absorption events, involving aggregates of nanoparticles, that lead to enhanced absorption when the concentration is raised. Simulations provide a description of the phenomenon that is compatible with experiments and constitute a way to understand and estimate the absorption and scattering cross-sections of both dispersed particles and/or aggregates. A comparison of experiments and simulations suggests that there is some aggregation of the gold nanoparticles by forming clusters of about 2–7 particles, but no information about their structure can be obtained without further theoretical and experimental developments. This nonlinear behavior could be useful to get very high ETP velocities by inducing some controlled aggregation of the particles.

1. Introduction

There are many applications based on lab-on-a-chip technologies that involve the transport and mixing of fluids inside microchannels [1–3], but fulfilling their demands requires further developments. One hurdle to be overcome is due to the fact that mixing essentially occurs by diffusion, which is inherently slow [4]. Moreover, laminar flow is typically present at the microscale due to the small Reynolds numbers attained, so convection has to be actively forced in order to speed up mixing. This is particularly important in the case of applications based on surface sensors [5,6] or where mixing between different species is intended [7]. Active pumping is also required in many applications, and the standard approach involves the use of syringe pumps that create pressure-driven flows [8–11]. However, miniaturization and portability clearly require the use of alternative approaches [12,13].

Convection can be triggered by strong temperature gradients. These can be obtained e.g. via light-to-heat conversion with plasmonic nanostructures deposited on a substrate [14–21]. Likewise, electrokinetic techniques have been extensively developed both to induce convection and pump flow inside microchannels [22–27]. Nevertheless, these approaches present some drawbacks that prevent widespread application. In the case of plasmonic structures, the generation of strong flows requires somehow high-temperature increments (tens of K), which can compromise their use with analytes of biomedical interest, since most of them are very sensitive to temperature variations. On the other hand, electrokinetic pumps require high electric fields for their efficient operation [28–30]. Moreover, both approaches require costly microfabrication techniques.

Alternatively, electrothermal flow can be efficiently generated by combining a small temperature gradient with an AC electric field [31–33]. A plasmonic nanostructure used as a heat source in combination with an AC electric field has been shown to provide versatility in the generation of convective flow inside microchannels thanks to the electrothermoplasmonic (ETP) effect [34–37]. This approach is attractive since the ETP effect has been shown to provide significant flow with low-temperature increments and moderate electric fields. Interestingly, the flow thus obtained can be even engineered to create stagnation points that are able to trap molecules and small nanoparticles in a region where no heating is produced [38].

In this work, we explore a novel configuration for ETP flow where heating is achieved thanks to the laser absorption of plasmonic gold nanoparticles dispersed in the fluid, which constitutes an interesting

* Corresponding author at: Universidad de Málaga, Department of Applied Physics II, 29071, Málaga, Spain.
E-mail address: eruizr@uma.es (E. Ruiz-Reina).

https://doi.org/10.1016/j.jcis.2023.05.198
Received 12 January 2023; Received in revised form 22 May 2023; Accepted 31 May 2023
Available online 7 June 2023

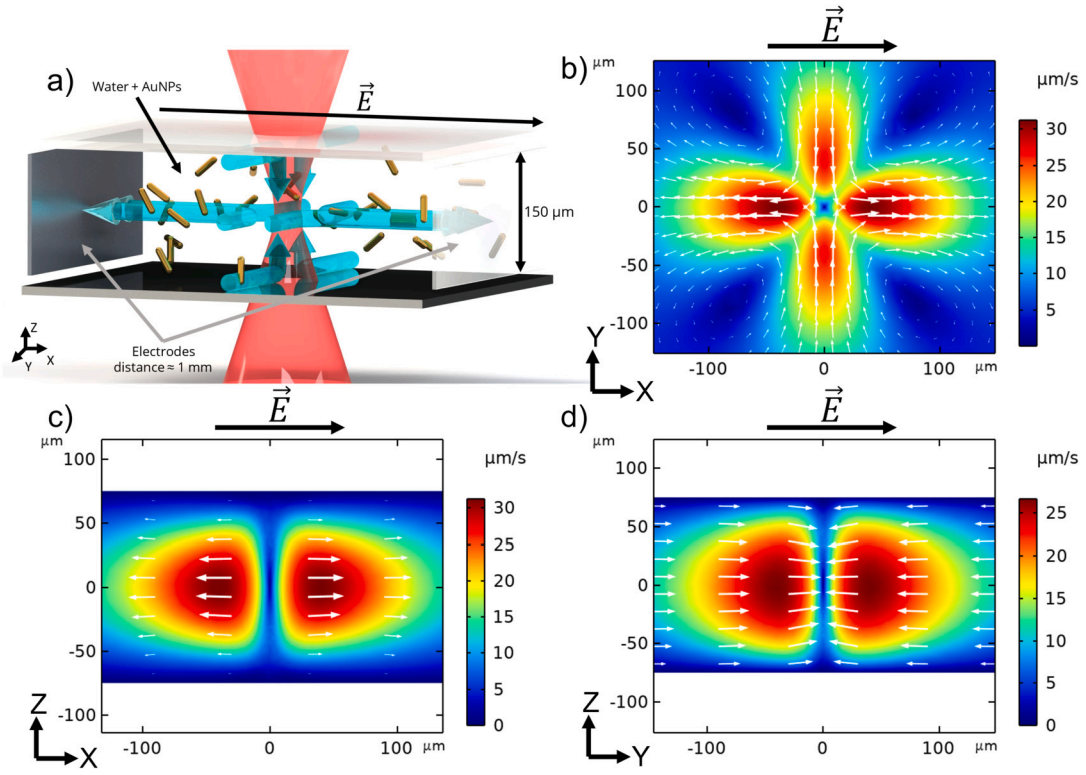

Fig. 1. Schematic representation of the problem and simulations of the fluid-velocity field. (a) A microfluidic chamber is fabricated by sandwiching two aluminum-foil electrodes with two glass coverslips. An infrared laser ($\lambda = 980$ nm) is focused by an objective microscope (20x, NA = 0.4), and excites off-resonance the surface plasmon of gold nanoparticles (AuNPs) uniformly dispersed in the bulk. An AC electric field is generated in the bulk by feeding the electrodes with an AC voltage signal ($f = 100$ kHz) between two electrodes (typical distance ≈ 1 mm, see panel (a)) that apply an oscillating electric field with intensity in the range 10–50 V/mm. The blue arrows in panel (a) represent the direction of the fluid flow in the chamber. Panels (b), (c), and (d) show the simulated flow fields in the XY, XZ, and YZ planes, respectively. In the simulations, the AuNP concentration is $4.96 \cdot 10^{12}$ particles/cm^3, the incident laser power is 30 mW and the applied electric field is 30 V/mm. (For interpretation of the colors in the figure(s), the reader is referred to the web version of this article.)

alternative to the deposition of gold nanostructures on a substrate [16,36]. This platform is used to better understand and characterize the dynamics of ETP flow. In our experiments, we present measurements of the flow field obtained as a function of the electric field, the laser power, and the concentration of dispersed gold nanoparticles (AuNPs). We compare our results with simulations performed with COMSOL Multiphysics, providing an in-depth understanding of the mechanism behind ETP flow.

The paper is organized as follows. We first introduce ETP fundamentals, discussing the particular structure of ETP flow obtained in our configuration aided by computer simulations. Further, we present experimental results of the flow field obtained under different experimental situations, comparing these with simulations. Finally, we present simulations of the scattering cross-section of aggregates of plasmonic nanoparticles, and discuss why they are needed to justify the observed behavior.

2. Overview of electrothermoplasmonic flow

The electrothermal effect is a flow generation technique that combines a gradient of temperature $\nabla T(\mathbf{r})$ with an applied AC electric field $\mathbf{E}$. In this situation, the electric field exerts a body force on the fluid due to gradients in electric permittivity and conductivity concomitant with the temperature gradient. The driving electrothermal force at position $\mathbf{r}$ is [31]:

$$\mathbf{F}_{\mathrm{ET}}(\mathbf{r}) = \frac{1}{2}\mathrm{Re}\left[\frac{\varepsilon(\alpha-\beta)}{1+i\omega\tau}(\nabla T(\mathbf{r})\cdot\mathbf{E})\mathbf{E}^* - \frac{1}{2}\varepsilon\alpha|\mathbf{E}|^2\nabla T(\mathbf{r})\right] \quad (1)$$

where $\alpha = (1/\varepsilon)(\partial\varepsilon/\partial T)$, $\beta = (1/\sigma)(\partial\sigma/\partial T)$, and σ and ε are the conductivity and permittivity of the solution, respectively, at the angular frequency ω of the electric field. The second term in this body force starts to dominate over the first one above the MHz range, determined by the inverse of the relaxation time of the solution $1/\tau = \sigma/\varepsilon$ [31,36].

The configuration we have used is depicted in Fig. 1a). In our experiment, the temperature gradient is obtained via resonant excitation of surface plasmons in gold nanoparticles that are dispersed in the fluid [21]. This is different from previous approaches, where ETP flow was generated by the excitation of nanostructures deposited on a surface [35,36]. Therefore, the geometry of the convection cells we obtain is different, since in our case the electric field is perpendicular to the laser beam (see Fig. 1a)), while in previous works the laser and the electric field were always parallel [35–37]. Experiments and numerical simulations based on finite element analysis and performed with COMSOL Multiphysics (see Methods section) reveal that the flow field features a quadrupolar structure in the focal plane (XY). The liquid flows inwards (outwards) from (to) the focus in the directions perpendicular (parallel) to the electric field, respectively (see Fig. 1). Interestingly, the flow is significant, leading to vortexes moving at tens of µm/s over distances hundreds of microns apart from the focus, what can be useful in mixing applications.

3. Methods

3.1. Experimental

A microfluidic chamber is constructed by sandwiching two electrodes made of aluminum foil (150 ± 20 µm thickness) with two glass coverslips (thickness 170 ± 5 µm). The typical distance between electrodes is 1 mm. During an initial exploration, we tested different ways to build the microchambers, also using ITO coverslips with 120 µm

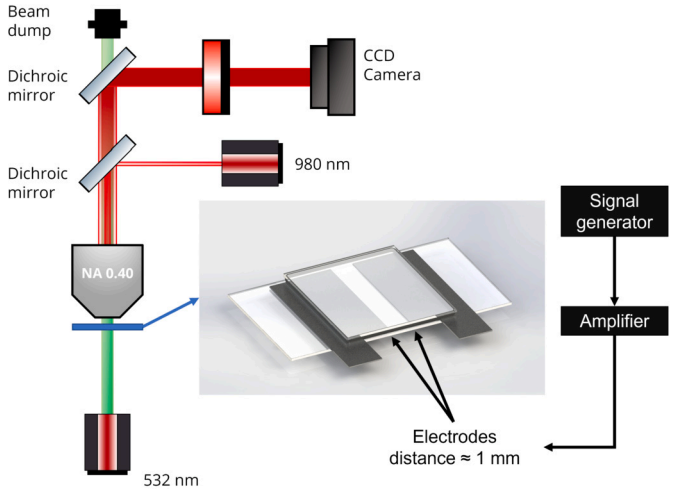

Fig. 2. Optical setup. Notice the microfluidic chamber and electrodes in the center, as well as the electric scheme on the right.

spacers. However, this approach changes the direction of the electric field and hence of the flow pattern, making it difficult to reliably measure the velocity. Simulations of the expected results are provided at the end of the manuscript.

We have prepared suspensions of a mixture of plasmonic nanoparticles and fluorescent microparticles in water. The nanoparticles are used to generate the temperature gradient, while the fluorescent microparticles serve as flow tracers. The flow tracers move with a velocity $\mathbf{v} = \mathbf{u} + \mathbf{F}/\gamma$, where $\mathbf{u}$ is the velocity of the flow, $\mathbf{F}$ is the sum of the external forces acting on the particles and $\gamma = 6\pi\eta r$ is the Stokes friction coefficient, which depends on the fluid viscosity η and the tracer particle radius r. Since the electric field is AC and with negligible gradients in our electrode configuration, we can safely ignore additional forces on the particles and identify the velocity of the fluid with that of the tracers.

We have built a fluorescence microscope to track the trajectory of the flow tracers. The scheme is shown in Fig. 2. Briefly, a laser beam ($\lambda = 532$ nm) has been used to excite the fluorescence of the tracer microparticles (diameter 500 nm, from Sigma Aldrich). A $\lambda = 980$ nm laser from Arroyo Instruments has been focused to a diffraction-limited spot (diameter 1.56 μm) incident toward the sample to excite AuNPs, and an electric field has been applied with a signal generator from RSPro RSDG 1032X and an amplifier from Falco Systems WMA-100 as can be seen in Fig. 2. The experiments were recorded with an IDS UI 1240 CMOS camera and a NAVITAR 50 mm lens.

The gold nanoparticles used were rods with 16 ± 4 nm mean diameter, 56 ± 9 nm mean length, and average aspect ratio of 3.7 ± 0.8, where the estimates have been obtained from TEM images of 70 particles and uncertainties indicate standard deviation [39] (see also Supplementary Images). Sizing of the AuNPs in suspension by means of dynamic light scattering (Nanosizer Nano ZS, Malvern Instruments) leads to the results shown in Fig. 3a). In this case, we detect 2 populations present, namely, a broad peak centered at about 6 nm and another one at about 85 nm. The lower peak does not correspond to a population of small nanoparticles, but is due to the rotational diffusion of non-spherical particles. On the other hand, the higher peak should be attributed to the size of an equivalent sphere having the same diffusion coefficient as the rods. This can be calculated as $d_{\text{eff}} = \sqrt{L^2/12 + R^2/2}$ [40]. For our rods, this formula predicts $d_{\text{eff}} \simeq 17$ nm, which does not agree with any of the populations retrieved in the DLS measurements. This indicates that our sample presents some degree of aggregation, as we discuss below. This aggregation is present in suspensions independently from ETP experiments.

As can be seen in the experimental extinction curve (see Fig. 3b)) suspensions of these particles have a plasmon resonance at a wavelength of around 850 nm. This resonance is also consistent with some

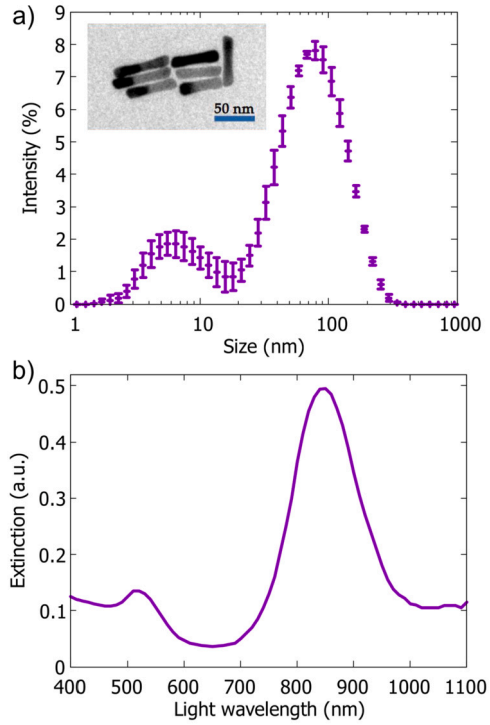

Fig. 3. a) DLS measurements of aqueous suspensions of the AuNPs. Error bars stand for the standard deviation obtained from 5 independent measurements. The inset is a high-resolution TEM picture of gold nanoparticles (AuNPs) sample. b) Extinction (scattering + absorption) spectrum of the gold nanorods suspension [39].

level of aggregates present in suspension since we expect from previous works and simulations that the resonant peak for our gold rods should be centered at a wavelength between 750 nm and 800 nm [41–43]. We choose the laser wavelength used in the ETP experiments to be 980 nm, away from the resonance in order to avoid excessive heating and thus generate a moderate temperature gradient.

Videos of the flow motion have been recorded on the CMOS camera and analyzed with PIVLab [44,45] to produce experimental flow fields. In order to achieve a reasonable signal-to-noise ratio, we have recorded videos of, at least, 200 frames. Each of them was analyzed to obtain a velocity field with an interrogation area of 64×64 pixels^2. Averaging out over the frames, we obtain a mean velocity field that is used to evaluate performance.

3.2. ETP simulations

Additionally, to test the theoretical expression for the ETP driving force [35], we have performed COMSOL Multiphysics numerical simulations. With these simulations we have solved the strongly coupled heat transfer (Eq. (2)), Navier-Stokes (Eq. (3)), and Poisson (Eq. (4)) equations for calculating temperature, flow velocity, and electric fields.

$$\rho_l c_p \mathbf{u}(\mathbf{r}) \cdot \nabla T(\mathbf{r}) - \kappa \nabla^2 T(\mathbf{r}) = q(\mathbf{r}) \tag{2}$$

$$\nabla[p(\mathbf{r})\mathbf{I} - \mu(\nabla \mathbf{u}(\mathbf{r}) + (\nabla \mathbf{u}(\mathbf{r}))^T)] = \mathbf{F}(\mathbf{r})$$
$$\nabla \cdot \mathbf{u}(\mathbf{r}) = 0 \tag{3}$$

$$\nabla^2 \varphi = -\frac{\rho}{\varepsilon} \tag{4}$$

where $\mathbf{F}(\mathbf{r})$ is the electrothermal body force shown in Eq. (1). ρ_l, c_p, κ and μ are the volume density, specific heat capacity, thermal conductivity, and dynamic viscosity of the aqueous solution, respectively. $T(\mathbf{r})$, $\mathbf{u}(\mathbf{r})$ and $p(\mathbf{r})$ are the spatial temperature, fluid velocity, and fluid pressure fields, respectively $\mathbf{I}$ is the constant 3×3 identity matrix and the

superscript T denotes matrix transposition. In the Poisson equation, φ is the electric potential energy per unit charge, ρ is the total volume charge density and ε is the permittivity of the medium. The main heat source $q(\mathbf{r})$ comes from the region of the dispersed nanoparticles illuminated by the heating laser beam. We modeled the heat power per unit volume, P_{abs}, due to the AuNPs absorption with the following expression in cylindrical coordinates ρ_c and z [46]:

$$P_{\text{abs}} = \sigma_{abs} I(\rho_c, z)\text{Prob}[\rho_c, z] \tag{5}$$

where we assume that the intensity profile of the laser beam is:

$$I(\rho_c, z) = I_{inc}\left(\frac{W_0}{W(z)}\right)^2 \exp\left(-\frac{2\rho_c^2}{W^2(z)}\right) \tag{6}$$

with $W(z) = W_0\sqrt{1+(z/z_0)^2}$, $W_0 = \sqrt{\lambda z_0/n\pi}$ and $z_0 = \lambda n/(\pi(\text{NA})^2)$ are the beam width, waist radius, and the Rayleigh range, respectively. Also, σ_{abs} is the absorption cross-section of AuNPs and I_{inc} is the intensity at the center of the focal region ($\rho_c = z = 0$), while NA is the numerical aperture and n is the refractive index of water. Lastly, $\text{Prob}[\rho_c, z]$ corresponds to the AuNP concentration in the sample, which is assumed to be uniform. In Eq. (6), we implicitly assume that the relative absorption of light is low, given the fact that the absorption cross-section and the concentration of AuNPs are low. Therefore, the intensity profile is not affected by absorption but is only given by the properties of the focusing system.

3.3. Electromagnetic simulations

The ETP flow is generated by the combination of an applied AC electric field and a thermal gradient, the latter one a direct consequence of the incident laser energy absorption and scattering by the AuNPs (both as individual particles and as part of aggregates). This means that, in order to analyze the ETP flow behavior, we need as a first step the study of the absorption and scattering cross-sections. The heat power generated inside the AuNPs appears as an input to the calculation of the temperature and flow fields by solving the coupled heat transfer and momentum balance equations.

The absorption and scattering cross-section simulations are performed by the use of the finite-element analysis platform COMSOL Multiphysics, with an Electromagnetic Waves, Frequency Domain physics interface combined with a Wavelength Domain study. The physics interface provides different approaches to computing the electromagnetic fields in the whole system. In this case, we have solved only for the perturbation electric field arising from a background plane wave electric field $\mathbf{E}_b$ incident on the nanoparticles:

$$\mathbf{E}_b = \mathbf{E}_0 e^{i\mathbf{k}\cdot\mathbf{r}} \tag{7}$$

where $\mathbf{E}_0$ is the incident electric field amplitude, $\mathbf{k}$ is the wave number vector in water, and $\mathbf{r}$ is the position vector. The physics interface solves the following expression:

$$\nabla\times(\nabla\times\mathbf{E}) - \kappa_0^2\varepsilon_r\mathbf{E} = 0 \tag{8}$$

where κ_0 and ε_r are the free-space wave number and relative permittivity, respectively.

The geometry of all electromagnetic simulations, those shown in Figs. 6–8, is composed of a sphere representing a certain water domain and, depending on the simulation, one or more gold nanoparticles arbitrarily oriented and distributed close to the center of the sphere. The material of the nanoparticles is gold, with a wavelength-dependent complex refractive index, while the water domain has been simplified to a material model with an only-real part refractive index, with a value of $n_{water} = 1.33$. The water domain sphere is surrounded by a spherical shell with a PML (Perfectly Match Layer) setting. This shell has coordinates stretched out toward infinity to mimic an open and non-reflecting infinite domain that absorbs the outgoing waves, and so prevents reflections back into the region of interest. It is also prescribed a Scattering Boundary Condition in the external boundaries of the PML.

From the perturbation electromagnetic fields, we can compute the absorption σ_{abs} and scattering σ_{sc} cross-sections with the following expressions:

$$\sigma_{abs} = \frac{1}{I_0}\int_V Q_h = \frac{1}{I_0}\int_V \frac{1}{2}\mathbf{J}\cdot\mathbf{E}^* \tag{9}$$

$$\sigma_{sc} = \frac{1}{I_0}\int_S \mathbf{P}_{av}\cdot\mathbf{n} \tag{10}$$

where I_0 in the incident intensity, total power dissipation density, $\mathbf{J}$ is the electric current density in the nanoparticles, $\mathbf{E}^*$ is the complex conjugate of the perturbed electric field, $\mathbf{P}_{av}$ is the time-averaged perturbation Poynting vector, $\mathbf{n}$ is the surface normal, and V and S are the volume and surface of all nanoparticles, respectively.

4. Results and discussion

4.1. Experimental results on electrothermoplasmonic flow

In this section, we analyze experimentally the influence of the different parameters in the ETP flow, by evaluating the maximum velocity observed in each experiment. These are compared with simulations of the ETP flow. Similar results are obtained if the average velocity is considered instead of the maximum velocity.

We have performed multiple experiments in order to evaluate the dependencies of the flow field with the electric field, laser power, and gold nanoparticles concentration. The frequency of the AC field in these studies is kept at 100 kHz. This choice is based on the fact that the electrothermal flow has been shown to be independent of frequency in the range [10 kHz–1 MHz] [33,36]. This is the case when the condition $\varepsilon\omega/\sigma << 1$ is fulfilled, as is the case for suspensions made with CO_2 saturated water with no electrolytes added. Likewise, ETP flow is expected to be the main driving force in this regime, given the size of our chamber and the used electric field. Notice that other effects like AC electroosmosis can dominate fluid flow if the distance between the walls is decreased [33]. In simulations, AC electroosmosis is not included, but buoyancy is taken into account (see Methods). The lower frequency bound safely excludes electrolysis and polarization effects on the electrodes.

We first make a qualitative comparison between theory and simulations in Fig. 4. As can be seen, we experimentally observe the quadrupolar structure predicted by simulations (compare with Fig. 1). In this case, flow velocities as high as 60 μm/s are obtained with moderately low electric fields (30 V/mm). Even if our experimental setup does not allow us to measure the temperature of the fluid, comparison with simulations provides an estimate. Fig. 4b) also depicts the temperature field that matches the experiment in the left panel of Fig. 4. The simulation considers heat transfer and the intensity distribution of the focused Gaussian beam [46]. As can be seen, the temperature field presents one lobe in the focus, where the fluid temperature is raised due to heat generation upon plasmonic excitation. Interestingly, simulations predict that just a 4.5 K temperature increment at the focus is enough to develop convection cells with the observed velocities.

We have checked that the numerical aperture and power of the laser beam, and also the electric field intensity, do not affect significantly the shape or size of the quadrupolar vortices. It seems that the size of the vortices is governed essentially by geometrical restrictions, as we have found that increasing the height of the simulation domain involves an enlargement of the vortices. This behavior is related to the available space for these structures to develop. The experimental uncertainty in the true height of the measuring cell can explain the small discrepancies observed about the spatial extent of the quadrupolar shape comparing Figs. 4a) and 1b). Moreover, an imperfect matching of the laser focus plane and the observation plane could also contribute to small discrepancies in the observed size of the lobes.

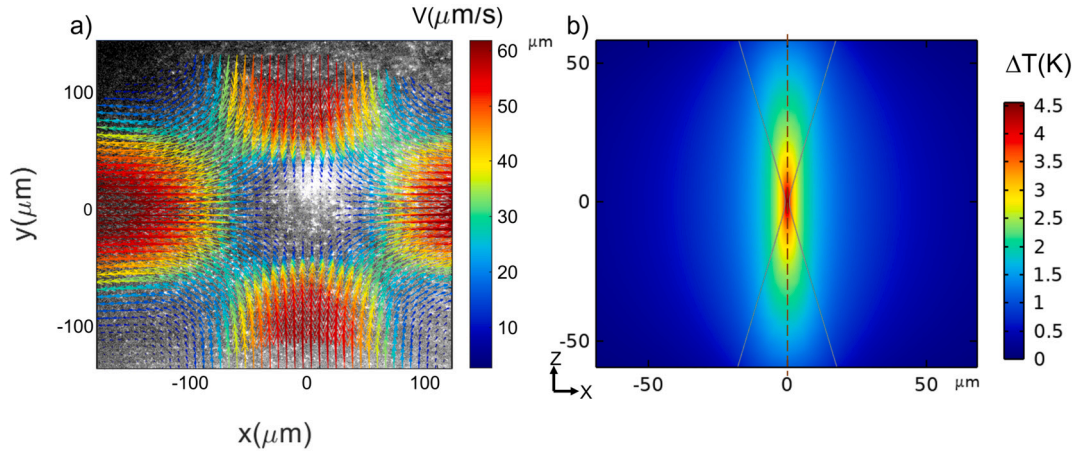

Fig. 4. Left: Experimental flow field. The AuNP concentration is $4.96 \cdot 10^{12}$ particles/cm^3, the incident laser power is 30 mW and the applied electric field is 30 V/mm. Right: Simulated temperature increment corresponding to the experimental condition shown on the left. The gray line corresponds to the laser beam profile.

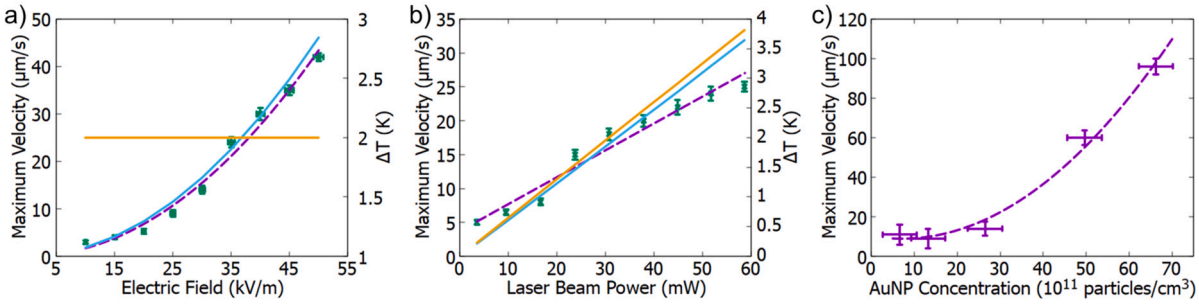

Fig. 5. a) Experimental data (*dots*), experimental fit (*dashed line*), and simulation results (*blue solid line*) of maximum flow velocity for an incident laser power of 30 mW and different applied electric fields. The orange solid line is the maximum temperature increment, as obtained from simulations. b) Experimental data (*dots*), experimental fit (*dashed line*) and simulation results (*blue solid line*) of maximum flow velocity for an applied electric field of 30 V/mm and different incident laser power. The orange solid line is the maximum temperature increment, as obtained from simulations. Concentration for panels a and b are $2.6 \cdot 10^{12}$ particles/cm^3. c) Experimental maximum flow velocity (dots) for different AuNP concentrations and an applied electric field of 30 V/mm and an incident laser power of 30 mW. The dashed line is an experimental fit.

In order to characterize the performance of ETP flow, we have done experiments analyzing the influence of electric field magnitude, excitation laser power, and particle concentration. The results are shown in Fig. 5a), b), and c). For each experimental condition, one video was recorded; except for the curve shown in Fig. 5c) where two videos were recorded. The particle concentration value for the data in Figs. 4, 5a), 5b) was the same as in Fig. 1. We first analyze the effect of the applied electric field. Fig. 5a) shows that the maximum velocity scales quadratically on the applied electric field, as expected for ET flow (see Eq. (1)). Likewise, in Fig. 5b), where the applied electric field is fixed, the relationship between the flow field and the generated heat is linear as expected from Eq. (1). The temperature increment raises with the infrared laser power, leading to an ever-increasing velocity. Deviations from linearity are likely due to variability in the construction of the flow chambers.

Together with the experiments, we present the results of the simulations. For this aim, the only unknown input is the absorption cross-section of the particles in suspension, which we used as a fitting parameter. Since our gold nanoparticles have a tendency to aggregate [39], a direct theoretical estimation of this value from simulations is not feasible, as we discuss later. In order to get a consistent analysis, we have performed all the simulations with the same value of the absorption cross-section, which is considered a fitting parameter and will be discussed later. Therefore, all ETP flow simulations have been performed using a fitted value of $2.5 \cdot 10^{-17}$ m^2 for the absorption cross-section. With this value, the agreement between the predictions of the simulations and the experimental results is adequate in all cases.

Finally, we characterize the influence of the concentration of AuNPs on the flow velocity. We have performed experiments with five different concentrations at a fixed electric field and laser intensity. The results are shown in Fig. 5c), where we observe that the maximum velocity has a quadratic dependence on particle concentration. Velocities as high as 100 μm/s are observed at moderate values of electric field and laser power, and we estimate that up to 0.5 mm/s could be achieved with the maximum values of electric field and laser power we tested in our set of experiments. However, we could not measure adequately this value due to the limited acquisition speed of our camera (25.8 fps for the full sensor).

The origin of this nonlinearity is unclear, but we hypothesize that it has to do with the way photons are scattered and absorbed by the AuNPs. Proper modelling of the propagation of the laser beam through the sample would involve the solution of an equation of energy transfer, which is out of the scope of this work [47,48]. However, some considerations can be made in order to get information from this result. For purely absorbing media, the Beer-Lambert law predicts that the absorption of light should increase linearly with concentration. In this situation, increasing the concentration of AuNPs would have a similar effect on the velocity as the increase of laser power, and the dependence should be linear, which is not the case. Therefore, in order to account for the observed non-linearity, we need to consider multiple scattering events [47]. A photon that interacts with a NP can be either scattered or absorbed, with a probability that depends on the respective cross-section. When the concentration increases, a scattered photon is likely to interact with neighboring particles, increasing its probability to be absorbed. Scattering-absorption events are likely to enhance the

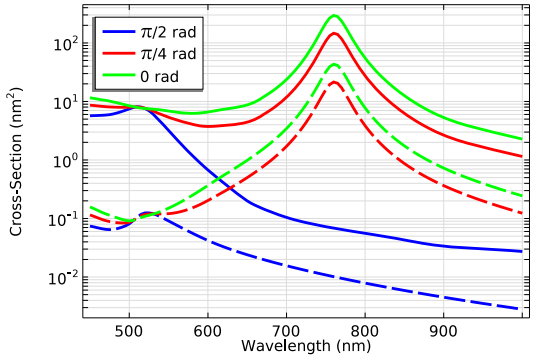

Fig. 6. Absorption (solid) and scattering (dashed) simulated cross-section spectra of a single gold nanoparticle for different angles θ between the incident electric field polarization and the AuNP major axis.

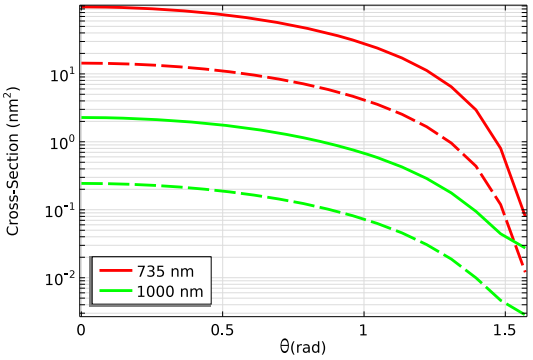

Fig. 7. Absorption (solid) and scattering (dashed) simulated cross-sections of a single gold nanoparticle as a function of the angle θ between the incident electric field polarization and the AuNP major axis.

absorbance of the suspension as particle concentration increases beyond the linear regime when the scattering and absorption cross-sections are comparable in magnitude [47]. As we will show later, at the particle concentration considered, this could happen when there is certain aggregation present in the suspension. In order to explore this possibility, we need to study the scattering and absorption cross-sections of the AuNPs used in our experiments, both as individual particles or being part of aggregates. Since we do not have a direct method to measure them, we performed numerical simulations, as described in the next section.

4.2. Absorption and scattering cross-sections

At this point, we must first consider whether there appears any collective heating effect that could take place in our system of nanorods. This effect has been predicted and observed previously in the case of different nanoparticle 1D and 2D periodic arrays [49]. In the present study, the maximum concentration used was $6.6 \cdot 10^{12}$ particles/cm^3, and this corresponds to an average distance between AuNPs of 660 nm, which is about 12 times the largest dimension of the AuNP (16 nm × 56 nm). As it is indicated in [49], if the NP inter-distance is at least 4 or 5 times larger than the NP diameter, they are far enough apart that they can be considered optically independent. We can improve this analysis a bit by estimating the parameter ζ defined in [49], which provides an empiric discriminator between collective ($\zeta \ll 1$) and individual regimes ($\zeta > 1$). Since there is no closed-form analytical expression for the 3D case, we could use the 2D expression $\zeta_2 = p^2/(3LR)$ (Eq. (22) in ref. [49]) to get an idea of what heating regime our system is in. If we consider $p \approx 660$ nm, $R \approx 20$ nm and $L \approx 1560$ nm (diffraction-limited spot diameter), we get $\zeta_2 \approx 4.7 > 1$, which is indicative of individual heating regime. Therefore, we are always in a situation where our AuNPs can be considered optically independent and we should not expect any collective heating behavior if they remain as individual nanoparticles (i.e., not aggregated). In our case, it only makes sense for a collective heating effect to appear just within the particles that compose an aggregate.

First, we have performed electromagnetic wave numerical simulations in the wavelength domain, using the finite-element analysis COMSOL Multiphysics platform to calculate the absorption and scattering cross-sections of an individual AuNP, which is modeled as a cylinder with rounded bases, 56 nm length and 16 nm diameter [39]. The numerical results obtained are shown in Figs. 6–7.

The highest calculated plasmon resonance peak is located at a frequency of about 780 nm. This result is not in agreement with the experimental absorption spectra of our nanorods suspension, see Fig. 3, while it fits previous results obtained with similar particles [42]. Experimentally, the main resonance peak appears around 850 nm wavelength and is much broader. This disagreement indicates that our suspension cannot be constituted by individual nanoparticles well separated within the aqueous medium. The reason for this discrepancy lies in the presence of a certain level of particle aggregation, as will be discussed later.

It is straightforward that the energy absorption and scattering magnitudes depend strongly on the relative orientation angle θ between the incident electric field polarization and the AuNP major axis, *i.e.*, $\sigma = \sigma(\theta)$, being $\theta \in [0, \pi/2]$, as can be observed in Fig. 6 and more clearly in Fig. 7. As expected, the cross-section values are higher when the electric field of the wave is parallel to the major axis of the AuNP ($\theta = 0$), and minimum when it is parallel to the diameter ($\theta = \pi/2$). The laser source used in experiments emits unpolarized light, and the AuNPs are subjected to both random translational and rotational Brownian motions. As a consequence, the actual cross-sections for an individual particle should be compared or estimated by an average, over all possible angles θ, of the calculated cross-section magnitudes.

Previous numerical calculations of the laser scattering of different aggregates of nanorods [41,50] show that the absorption resonance peak position depends strongly on the number of particles of the aggregate and its spatial configuration. The explanation behind this phenomenon is that there is a strong interaction between the surface plasmons of neighboring particles that lead to a red shift and multiple resonances, even if the aspect ratio of the aggregate with respect to that of a single particle does not change. Similar results were obtained in our own test simulations, see Fig. 8, and we have found that the calculated resonance peaks wavelength shift to values much closer to the experimental broad resonance peak (850 nm, Fig. 3) than that of an individual nanoparticle (780 nm, Fig. 6). Also, we show that the relative magnitude of the resonance peaks depends strongly on the specific configuration of the aggregate.

Another remarkable finding is that, in the case of aggregates, the scattering cross-section is now a larger percentage relative to the absorption cross-section (about 40%–60%), than that found in the case of an individual nanoparticle (a maximum of 14%, Fig. 6). This reflects the occurrence of multiple scattering-absorption events, which would be very unlikely in the case of isolated particles at the considered concentrations in the experiments.

If we consider that our system is a collection of aggregates, with a variable number of nanoparticles and random configurations, then the measured extinction spectra should be compared with an average over all aggregation possibilities (in Fig. 8 there are a few) with weights corresponding to the suspension aggregation statistics. Inspecting the numerical results in Fig. 8, it is clear that the weighted superposition of all these possible spectra would result in a curve quite close to the experimental one, Fig. 3, with the broad resonance peak at 850 nm.

We then conclude here that: i) there is a certain level of particle aggregation in our system, and that ii) it is not possible to obtain a good theoretical estimate of the absorption cross-section without much more detailed information on the configuration and aggregation statistics. Furthermore, the presence of this aggregation can be observed in the TEM image in the inset of Fig. 3, although it is not clear that it

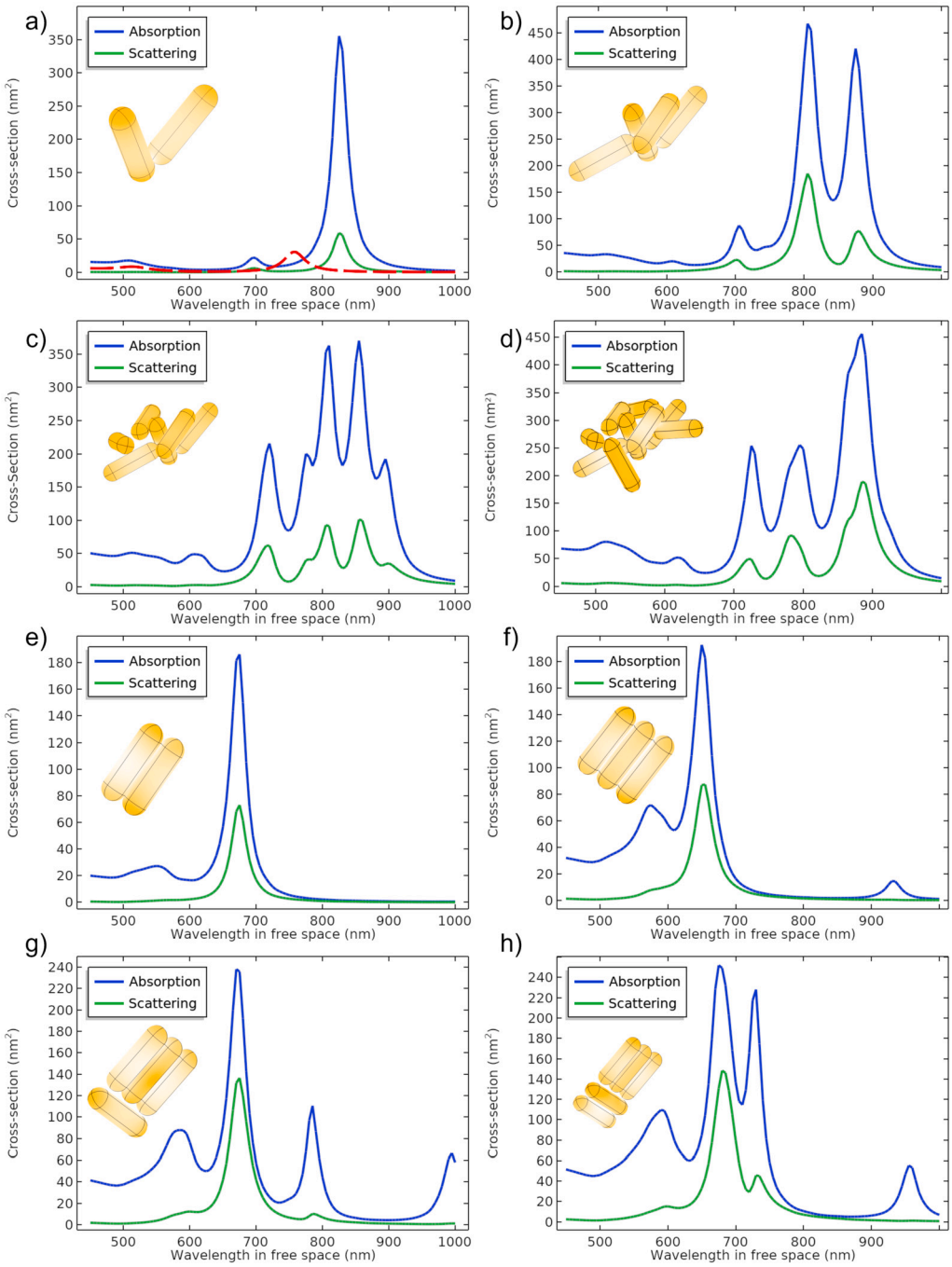

Fig. 8. Absorption and scattering cross-sections for random aggregates of a) 2 nanoparticles, b) 4 nanoparticles, c) 6 nanoparticles, and d) 9 nanoparticles. For reference, the absorption (red-dashed line) cross-section for an individual nanoparticle has been included in a). Also, the absorption and scattering cross-sections for orderly distributed aggregates of e) 2 nanoparticles, f) 3 nanoparticles, g) 4 nanoparticles and h) 5 nanoparticles. Insets: sketches for every aggregate configuration.

may also be due to the TEM preparation itself (see also Supplementary Images). Therefore, the effective absorption cross-section should be considered a fitting parameter, as we did in the previous section. The ETP flow simulations have been performed using a fitted value of $2.5 \cdot 10^{-17}$ m^2 for the absorption cross-section, being this value in good agreement with the typical range provided by the aggregate simulations for an incident vacuum wavelength of 980 nm.

4.3. Alternative configuration

For completeness, we have performed the simulations with the applied electric field parallel to the optical axis. This configuration is similar to the one presented in Ref. [36], only differing in the fact that in that case the gold particles were deposited on the substrate. The flow field structure now is composed of two superposed toroids, as can be seen in Fig. 9. Moreover, due to the height limitation (150 μm) the maximum velocities achieved are lower than those reported previously with the original electrode configuration. We have implemented experimentally this configuration with two ITO-covered glasses and performed measurements similar to the ones presented above, but in this case the tracking was difficult and we did not obtain reliable results.

5. Conclusions

We have performed a detailed analysis of ETP flow with a novel configuration, namely, with AuNPs dispersed in liquid instead of deposited

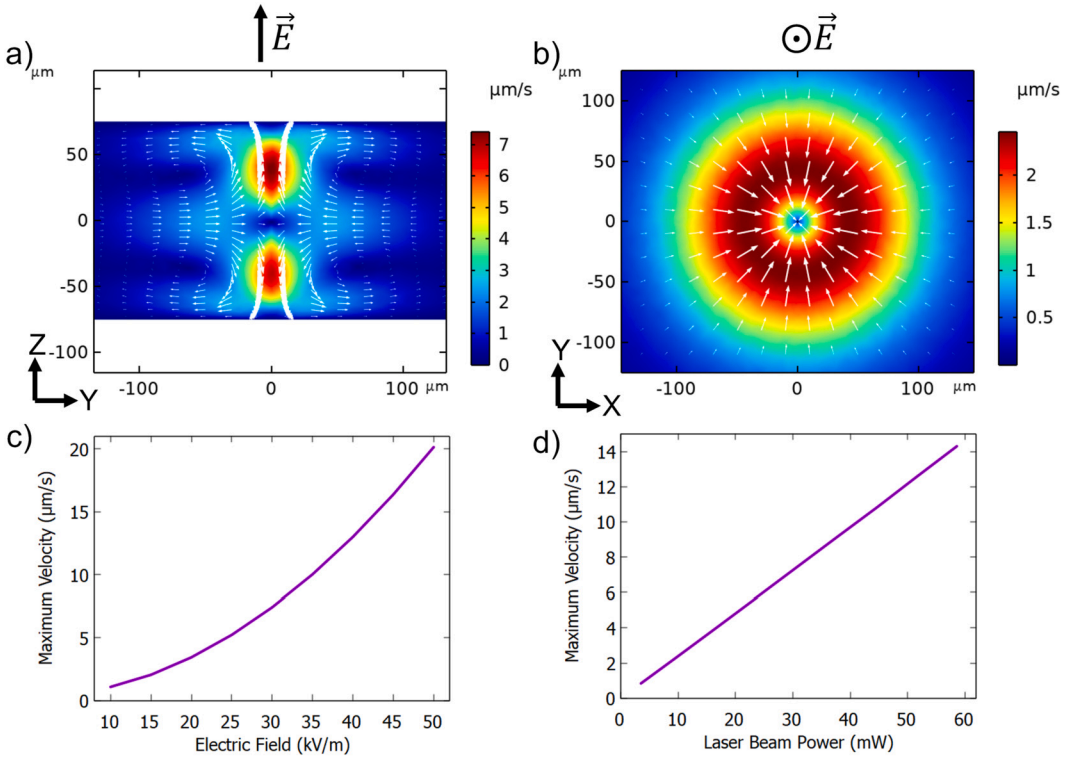

Fig. 9. Simulation results for an AC electric field applied parallel to the optical axis in the Z-direction. a) X-plane and b) Z-plane of electrothermoplasmonic flow patterns; c) maximum ETP velocity *vs* electric field intensity achieved with a constant laser power of 30 mW, and d) maximum ETP velocity *vs* laser beam power achieved with a fixed electric field amplitude of 30 V/mm. The concentration used for all the panels were $2.6 \cdot 10^{12}$ particles/cm^3.

on a 2D array. We have demonstrated that this configuration can lead to strong convection, which could be useful for mixing in microfluidic devices. We first have evaluated the effects of the electric field and laser power, finding good agreement with the simulations. This comparison allows us to obtain an estimation of the absorption cross-section of the AuNPs. The obtained value for the absorption cross-section suggests that the AuNPs in suspension are aggregated forming clusters, in agreement with the measurements from DLS and extinction. However, we could not get detailed information about their structure, but our results are consistent with clusters formed by 2–7 particles. Such clusters were also observed in TEM images.

We have demonstrated that the velocity scales quadratically with the concentration of AuNPs. While this dependence should be linear for purely absorbing particles at low concentrations, the presence of aggregates can be invoked to justify this nonlinearity. Two mechanisms can play a role in the observed behavior. On the one hand, it can happen that the scattering and absorption cross-sections become comparable in magnitude, so events of scattering and absorption become likely in the highest values of concentration. In this situation, absorption is enhanced, increasing the ETP flow. This is in agreement with the simulations we have performed since the magnitude of these two cross-sections becomes comparable in the case of aggregates. In contrast, the absorption cross-section is much larger than the scattering one in the case of isolated particles. On the other hand, increasing the concentration of nanoparticles in suspension can lead to ever larger aggregates, thus increasing the absorption cross-section and hence the overall absorption, leading to the observed nonlinearity. These two effects can be present simultaneously, but further work should be needed in order to distinguish between the two contributions. In any case, this nonlinear behavior could be very useful to get very high ETP velocities by inducing some controlled aggregation of the particles.

CRediT authorship contribution statement

Carlos David González-Gómez: Data curation, Formal analysis, Investigation, Software, Validation, Visualization, Writing – original draft, Writing – review & editing. **Raúl A. Rica:** Conceptualization, Funding acquisition, Investigation, Methodology, Project administration, Supervision, Writing – review & editing. **Emilio Ruiz-Reina:** Conceptualization, Investigation, Methodology, Software, Supervision, Writing – review & editing.

Declaration of competing interest

The authors declare that they have no known competing financial interests or personal relationships that could have appeared to influence the work reported in this paper.

Data availability

The data that support the findings of this study are available from the corresponding author upon reasonable request.

Acknowledgements

This research has been supported by Consejería de Universidad, Investigación e Innovación de la Junta de Andalucía and FEDER, “Una manera de hacer Europa”/Projects P18-FR-3583 and FQM-410-UGR18, Ministerio de Ciencia, Innovación y Universidades through Project EQC2018-004693-P, and Grant PID2021-127427NB-I00/ MCIN/AEI/ 10.13039/501100011033/FEDER,UE. Funding for open access charge: Universidad de Málaga/CBUA.

We thank Ángel Delgado and María L. Jiménez for providing the gold nanoparticles and for fruitful discussions.

Appendix A. Supplementary material

Supplementary material related to this article can be found online at https://doi.org/10.1016/j.jcis.2023.05.198.

References

[1] A. Hatch, E. García, P. Yager, Diffusion-based analysis of molecular interactions in microfluidic devices, Proc. IEEE 92 (1) (2004) 126–139.
[2] T. Gervais, K.F. Jensen, Transport and surface reactions in microfluidic systems, Chem. Eng. Sci. 61 (4) (2006) 1102–1121.
[3] T.M. Squires, R.J. Messinger, S.R. Manalis, Making it stick: convection, reaction and diffusion in surface-based biosensors, Nat. Biotechnol. 26 (4) (2008) 417–426.
[4] T.M. Squires, S.R. Quake, Microfluidics: fluid physics at the nanoliter scale, Rev. Mod. Phys. 77 (3) (2005) 977.
[5] P.E. Sheehan, L.J. Whitman, Detection limits for nanoscale biosensors, Nano Lett. 5 (4) (2005) 803–807.
[6] P.R. Roy, M. Tomkins, A. Docoslis, Enhancing the performance of surface-based biosensors by ac electrokinetic effects – a review, in: Pier Andrea Serra (Ed.), Biosensors – Emerging Materials and Applications, 2011, pp. 243–264.
[7] J. Marschewski, S. Jung, P. Ruch, N. Prasad, S. Mazzotti, B. Michel, D. Poulikakos, Mixing with herringbone-inspired microstructures: overcoming the diffusion limit in co-laminar microfluidic devices, Lab Chip 15 (8) (2015) 1923–1933.
[8] J.R. Lake, K.C. Heyde, W.C. Ruder, Low-cost feedback-controlled syringe pressure pumps for microfluidics applications, PLoS ONE 12 (4) (2017) 1–12.
[9] H.H. Richardson, M.T. Carlson, P.J. Tandler, P. Hernández, A.O. Govorov, Experimental and theoretical studies of light-to-heat conversion and collective heating effects in metal nanoparticle solutions, Nano Lett. 9 (3) (2009) 1139–1146.
[10] D.J. Laser, J.G. Santiago, A review of micropumps, J. Micromech. Microeng. 14 (6) (2004) R35.
[11] B.D. Iverson, S.V. Garimella, Recent advances in microscale pumping technologies: a review and evaluation, Microfluid. Nanofluid. 5 (2) (2008) 145–174.
[12] M. Schönberger, M. Hoffstetter, 6 – Emerging trends, in: M. Schönberger, M. Hoffstetter (Eds.), Emerging Trends in Medical Plastic Engineering and Manufacturing, William Andrew Publishing, 2016, pp. 235–268.
[13] S. Arshavsky-Graham, E. Segal, Lab-on-a-chip devices for point-of-care medical diagnostics, in: Microfluidics in Biotechnology, Springer International Publishing, Cham, 2020, pp. 247–265.
[14] J.S. Donner, G. Baffou, D. McCloskey, R. Quidant, Plasmon-assisted optofluidics, ACS Nano 5 (7) (2011) 5457–5462.
[15] B.J. Roxworthy, A.M. Bhuiya, S.P. Vanka, K.C. Toussaint Jr., Understanding and controlling plasmon-induced convection, Nat. Commun. 5 (1) (2014) 3173–3181.
[16] B. Ciraulo, J. García-Guirado, I. de Miguel, J.O. Arroyo, R. Quidant, Long-range optofluidic control with plasmon heating, Nat. Commun. 12 (1) (2021) 2001.
[17] G. Baffou, Thermoplasmonics: Heating Metal Nanoparticles Using Light, Cambridge University Press, 2017.
[18] A. Kotnala, P.S. Kollipara, J. Li, Y. Zheng, Overcoming diffusion-limited trapping in nanoaperture tweezers using opto-thermal-induced flow, Nano Lett. 20 (1) (2019) 768–779.
[19] Z. Chen, J. Li, Y. Zheng, Heat-mediated optical manipulation, Chem. Rev. 122 (3) (2021) 3122–3179.
[20] S.S. Aćimović, M.A. Ortega, V. Sanz, J. Berthelot, J.L. García-Cordero, J. Renger, S.J. Maerkl, M.P. Kreuzer, R. Quidant, Lspr chip for parallel, rapid, and sensitive detection of cancer markers in serum, Nano Lett. 14 (5) (2014) 2636–2641.
[21] G. Baffou, R. Quidant, Thermo-plasmonics: using metallic nanostructures as nano-sources of heat, Laser Photonics Rev. 7 (2) (2013) 171–187.
[22] A. Ramos, H. Morgan, N.G. Green, A. Castellanos, Ac electric-field-induced fluid flow in microelectrodes, J. Colloid Interface Sci. 217 (2) (1999).
[23] S. Zeng, C.-H. Chen, J.C. Mikkelsen Jr., J.G. Santiago, Fabrication and characterization of electroosmotic micropumps, Sens. Actuators B, Chem. 79 (2–3) (2001) 107–114.
[24] L.H. Olesen, H. Bruus, A. Ajdari, Ac electrokinetic micropumps: the effect of geometrical confinement, faradaic current injection, and nonlinear surface capacitance, Phys. Rev. E 73 (2006) 056313.
[25] C.C. Chang, R.J. Yang, Electrokinetic mixing in microfluidic systems, Microfluid. Nanofluid. 3 (5) (2007) 501–525.
[26] P. García-Sanchez, A. Ramos, N.G. Green, H. Morgan, Traveling-wave electrokinetic micropumps: velocity, electrical current, and impedance measurements, Langmuir 24 (17) (2008) 9361–9369.
[27] M.Z. Bazant, T.M. Squires, Induced-charge electrokinetic phenomena, Curr. Opin. Colloid Interface Sci. 15 (3) (2010) 203–213.
[28] X. Wang, C. Cheng, S. Wang, S. Liu, Electroosmotic pumps and their applications in microfluidic systems, Microfluid. Nanofluid. 6 (2) (2009) 145–162.
[29] M.K. Manshadi, M. Mohammadi, M. Zarei, M. Saadat, A. Sanati-Nezhad, Induced-charge electrokinetics in microfluidics: a review on recent advancements, J. Micromech. Microeng. 30 (11) (2020) 113001.
[30] L.J. Weiß, E. Music, P. Rinklin, M. Banzet, D. Mayer, B. Wolfrum, On-chip electrokinetic micropumping for nanoparticle impact electrochemistry, Anal. Chem. 94 (33) (2022) 11600–11609.
[31] A. Ramos, H. Morgan, N.G. Green, A. Castellanos, Ac electrokinetics: a review of forces in microelectrode structures, J. Phys. D, Appl. Phys. 31 (18) (1998) 2338–2353.
[32] N.G. Green, A. Ramos, A. González, A. Castellanos, H. Morgan, Electrothermally induced fluid flow on microelectrodes, J. Electrost. 53 (2) (2001) 71–87.
[33] A. Castellanos, A. Ramos, A. González, N.G. Green, H. Morgan, Electrohydrodynamics and dielectrophoresis in microsystems: scaling laws, J. Phys. D, Appl. Phys. 36 (20) (2003) 2584.
[34] J.C. Ndukaife, A. Mishra, U. Guler, A.G.A. Nnanna, S.T. Wereley, A. Boltasseva, Photothermal heating enabled by plasmonic nanostructures for electrokinetic manipulation and sorting of particles, ACS Nano 8 (9) (2014) 9035–9043.
[35] J.C. Ndukaife, A.V. Kildishev, A.G.A. Nnanna, V.M. Shalaev, S.T. Wereley, A. Boltasseva, Long-range and rapid transport of individual nano-objects by a hybrid electrothermoplasmonic nanotweezer, Nat. Nanotechnol. 11 (1) (2016) 53–59.
[36] J. García-Guirado, R.A. Rica, J. Ortega, J. Medina, V. Sanz, E. Ruiz-Reina, R. Quidant, Overcoming diffusion-limited biosensing by electrothermoplasmonics, ACS Photonics 5 (9) (2018) 3673–3679.
[37] C. Hong, S. Yang, I.I. Kravchenko, J.C. Ndukaife, Electrothermoplasmonic trapping and dynamic manipulation of single colloidal nanodiamond, Nano Lett. 21 (12) (2021) 4921–4927.
[38] C. Hong, S. Yang, J.C. Ndukaife, Stand-off trapping and manipulation of sub-10 nm objects and biomolecules using opto-thermo-electrohydrodynamic tweezers, Nat. Nanotechnol. 15 (11) (2020) 908–913.
[39] P. Arenas-Guerrero, Electro-optical behaviour of non-spherical particles under alternating fields, PhD Thesis, Universidad de Granada, 2018.
[40] J. Rodríguez-Fernández, J. Pérez-Juste, L.M. Liz-Marzán, P.R. Lang, Dynamic light scattering of short au rods with low aspect ratios, J. Phys. Chem. C 111 (13) (2007) 5020–5025.
[41] P.K. Jain, K.S. Lee, I.H. El-Sayed, M.A. El-Sayed, Calculated absorption and scattering properties of gold nanoparticles of different size, shape, and composition: applications in biological imaging and biomedicine, J. Phys. Chem. B 110 (14) (2006) 7238–7248.
[42] G.S. He, J. Zhu, K.-T. Yong, A. Baev, H.-X. Cai, R. Hu, Y. Cui, X.-H. Zhang, P.N. Prasad, Scattering and absorption cross-section spectral measurements of gold nanorods in water, J. Phys. Chem. C 114 (7) (2010) 2853–2860.
[43] J. Li, S. Liu, Y. Liu, F. Zhou, Z.-Y. Li, Anisotropic and enhanced absorptive nonlinearities in a macroscopic film induced by aligned gold nanorods, Appl. Phys. Lett. 96 (26) (2010) 263103.
[44] W. Thielicke, E. Stamhuis, Pivlab–towards user-friendly, affordable and accurate digital particle image velocimetry in matlab, J. Open Res. Softw. 2 (1) (2014).
[45] W. Thielicke, R. Sonntag, Particle image velocimetry for matlab: accuracy and enhanced algorithms in pivlab, J. Open Res. Softw. 9 (1) (2021).
[46] H. Rodríguez-Rodríguez, G. Salas, J.R. Arias-González, Heat generation in single magnetic nanoparticles under near-infrared irradiation, J. Phys. Chem. Lett. 11 (6) (2020) 2182–2187.
[47] N.J. Hogan, A.S. Urban, C. Ayala-Orozco, A. Pimpinelli, P. Nordlander, N.J. Halas, Nanoparticles heat through light localization, Nano Lett. 14 (8) (2014) 4640–4645.
[48] T.G. Mayerhöfer, S. Pahlow, J. Popp, The Bouguer-Beer-Lambert law: shining light on the obscure, ChemPhysChem 21 (18) (2020) 2029–2046.
[49] G. Baffou, P. Berto, E. Bermúdez Ureña, R. Quidant, S. Monneret, J. Polleux, H. Rigneault, Photoinduced heating of nanoparticle arrays, ACS Nano 7 (8) (2013) 6478–6488.
[50] D. Pratap, R.K. Shah, S. Khandekar, S. Soni, Photothermal effects in small gold nanorod aggregates for therapeutic applications, Appl. Nanosci. 12 (7) (2022) 2045–2058.